



Article

Conformational Effects of Pt-Shells on Nanostructures and Corresponding Oxygen Reduction Reaction Activity of Au-Cluster-Decorated NiO_x@Pt Nanocatalysts

Dinesh Bhalothia ^{1,2,†} , Yu-Jui Fan ^{3,†} , Yen-Chun Lai ^{2,4} , Ya-Tang Yang ¹ , Yaw-Wen Yang ⁴ , Chih-Hao Lee ² and Tsan-Yao Chen ^{2,5,6,7,*}

¹ Institute of Electronics Engineering, National Tsing Hua University, Hsinchu 30013, Taiwan

² Department of Engineering and System Science, National Tsing Hua University, Hsinchu 30013, Taiwan

³ School of Biomedical Engineering, Taipei Medical University, Taipei 11031, Taiwan

⁴ National Synchrotron Radiation Research Center, Hsinchu 30007, Taiwan

⁵ Institute of Nuclear Engineering and Science, National Tsing Hua University, Hsinchu 30013, Taiwan

⁶ Hierarchical Green-Energy Materials (Hi-GEM) Research Center, National Cheng Kung University, Tainan 70101, Taiwan

⁷ Higher Education Sprout Project, Competitive Research Team, National Tsing Hua University, Hsinchu 30013, Taiwan

* Correspondence: chencaeser@gmail.com or tsanyao@mx.nthu.edu.tw; Tel.: +886-3-5715131 (ext. 34271); Fax: +885-3-5720724

† These authors contributed equally to this work.

Received: 5 June 2019; Accepted: 9 July 2019; Published: 11 July 2019



Abstract: Herein, ternary metallic nanocatalysts (NCs) consisting of Au clusters decorated with a Pt shell and a Ni oxide core underneath (called NPA) on carbon nanotube (CNT) support were synthesized by combining adsorption, precipitation, and chemical reduction methods. By a retrospective investigation of the physical structure and electrochemical results, we elucidated the effects of Pt/Ni ratios (0.4 and 1.0) and Au contents (2 and 9 wt.%) on the nanostructure and corresponding oxygen reduction reaction (ORR) activity of the NPA NCs. We found that the ORR activity of NPA NCs was mainly dominated by the Pt-shell thickness which regulated the depth and size of the surface decorated with Au clusters. In the optimal case, NPA-1004006 (with a Pt/Ni of 0.4 and Au of ~2 wt.%) showed a kinetic current (J_K) of 75.02 mA cm⁻² which was nearly 17-times better than that (4.37 mA cm⁻²) of the commercial Johnson Matthey-Pt/C (20 wt.% Pt) catalyst at 0.85 V vs. the reference hydrogen electrode. Such a high J_K value resulted in substantial improvements in both the specific activity (by ~53-fold) and mass activity (by nearly 10-fold) in the same benchmark target. Those scenarios rationalize that ORR activity can be substantially improved by a syngeneic effect at heterogeneous interfaces among nanometer-sized NiO_x, Pt, and Au clusters on the NC surface.

Keywords: oxygen reduction reaction; nanocatalysts; carbon nanotube; wet-chemical reduction method; Au-clusters; mass activity

1. Introduction

Fuel cells are expected to be commercially feasible to moderate deficiencies in natural energy resources without increasing the carbon footprint [1–4]. In spite of many fascinating features like noise-free operation, substantial reductions in pollution, and better efficiencies, the commercial viability of fuel cells is hindered by the substantially high energy barrier of oxygen reduction reactions (ORR) at the cathode [5,6]. To reduce the energy barrier to ORR, platinum (Pt)-based heterogeneous catalysts

seem to be the most effective material [7–9]. Due to the unaffordable costs and low storage potential of Pt, finding alternative materials for nanocatalysts (NCs) with comparable efficiencies to Pt is an inevitable step to bringing fuel cells into the market. Meanwhile, lower overpotential losses, long-term durability, pH working conditions, non-toxicity, and earth-abundant elements are fundamental physical and economic requirements for usable material combinations. Despite many efforts so far expended on the development of fuel cells, especially over the past two decades, many hurdles have yet to be overcome. Several Pt-alloys [10–12], including 3D-transition metals (Co, Ni, Cu, Fe, etc.) together with core shell nanostructures [13–15], bimetallic nanodendrites [16], nanowires [17], nano-onions, etc. [18], have been intensively studied in recent decades. In addition, great efforts have been geared towards size [19], shape [20], and composition [21] controls of Pt-based NCs to overcome the aforementioned challenges for preparing highly active ORR catalysts. Those studies laid a strong foundation to further fine-tune the electronic and chemical properties of NCs to extend ORR performances. Promising and efficient techniques, however, are still far away from attaining commercial standards.

Achieving a reconcilable balance between catalytic activity and noble-metal dosages when developing NCs for ORRs is still a challenging task. Core-shell structured heterogeneous NCs with a transition metal (e.g., Co, Ni, Zn, Ru, Fe, and Sn) in the core and a Pt shell seem to be the most effective design in terms of cost considerations and catalytic activities. In such configurations, the core crystal injects electrons (or forms a negative field) to the shell crystal via a combination of three major effects: A bifunctional mechanism [22] (using a variety of adsorption species), ligand effects (electron localization because of the electronegativity gap between two atoms) [23–25], and the lattice strain (differences in atomic arrangements between intraparticle domains) [26–28]. Moreover, such elements, owing to low-energy pathways, provide the opportunity for allocation and recombination kinetics of radicals (i.e., O^* , OH^* , and H^*) in H_2O and reduce durations of intermediate steps on NC surfaces. Meanwhile, the Pt-shell protects transition metals in the core from corrosive conditions at fuel cell cathodes.

The presence of Au in heterogeneous NCs offers electronic, geometric, and compositional effects to tune catalytically active sites that were found to be effective for ORR [29,30]. We further improved the ORR activities of such NCs via decorating strong electronegative atomic-scale Au clusters at the interface and on the surface of Pt-stacked transition metal nanocrystallites. Au clusters not only recover surface defects but also form indirect heterojunctions to the core crystal and localize valence electrons from neighboring atoms using strong electronegative forces. Meanwhile, Pt forms an unconformable shell, which protects the core crystal from corrosion and shares ORR pathways, including O_2 splitting and relocation kinetics of O-atoms, and thus avoids highly energetic intermediates and their associated kinetic penalties. Our previous work demonstrated a facile approach to trigger ORR activity via Pt-decorated core-shell structures [31–35]. Those ternary metallic NCs consisting of lower dosages of Pt showed distinct activity towards ORR facilitation but with reduced fabrication costs.

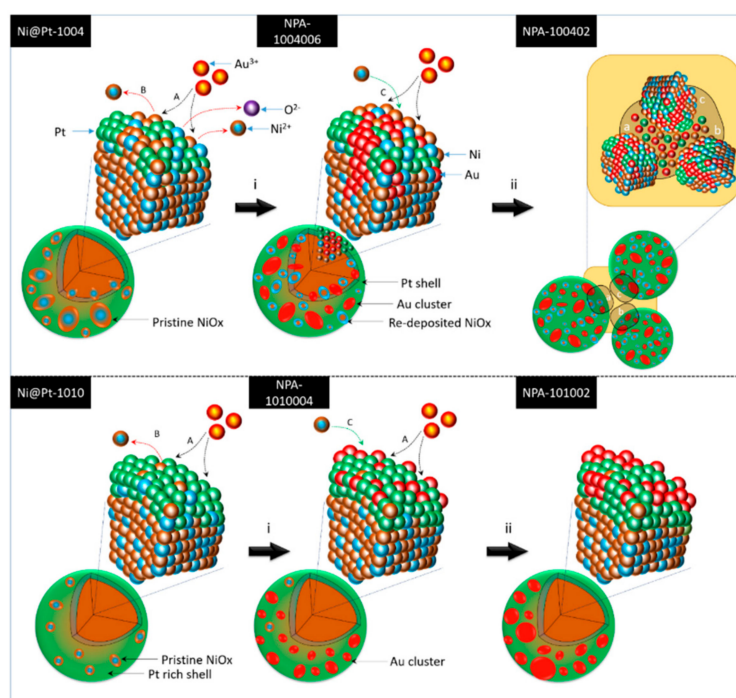
This study implemented an innovative sequence and time-controlled wet-chemical reduction method to synthesize Au cluster-decorated $Ni_{core}\text{-Pt}_{shell}$ NCs. The inner structure (heterogeneous intra-/interparticle interfaces and lattice strain) and surface coverage of such NCs were altered via changing the dosages of Au and Pt. In this event, a series of carbon nanotube (CNT)-supported ternary metallic NCs comprising a Ni/NiO_x core and an Au cluster-decorated Pt-shell (called NPA) were synthesized with variable shell thicknesses (with Pt/Ni ratios of 0.4 and 1.0) and Au contents (~2 and 9 wt.%) on the surface. Such synthesized NCs with unique multiphase cluster-in-cluster interfaces and surface modifications preserved improved catalytic activities towards ORRs in an alkaline environment (0.1 M KOH). Of greatest relevance, the mass activity (MA) and kinetic current density (J_k) of NPA-1004006 (with a Pt/Ni ratio of 0.4 and Au of ~2 wt.%) were improved by 10.36- and 17.16-fold, respectively, compared to those of commercial the Johnson Matthey-Pt/C (20 wt.% Pt) catalyst. At the same time, multiple metallic interfaces contributed to the lower electrochemical surface area (ECSA) with a shift of the Pt oxide reduction peak to more-positive potentials which thus improved the specific activity (SA) by 53.21-fold that of the commercial Johnson Matthey-Pt/C catalyst.

Herein, our findings present a proper strategy for the design of heterogeneous NCs by managing their local structure through controlling the surface and inner configurations. Systematic interpretations of the experimental results are given in latter sections.

2. Experimental

2.1. Synthesis Methodology and Materials for Preparing Ni Core-Pt Shell (Ni@Pt) NCs

Ni@Pt NCs were synthesized using a sequential wet-chemical reduction method [32]. Scheme 1 reveals the reaction steps of the synthesis methodology. Prior to NC synthesis, surface functionalization of catalyst support (multi-walled CNT (MWCNT), Cnano Technology Ltd., Beijing, China) was carried out via acid-treatment in 4.0 M H_2SO_4 at 80 °C for 6 h. In this way, the attachment of metallic crystals onto the CNT surface was strengthened. First, 500 mg of MWCNTs (5 wt.% solution in ethylene glycol (EG)) was added as catalyst support in 1.28 g of an aqueous solution, which contained 0.1 M nickel (II) chloride hexahydrate ($\text{NiCl}_2 \cdot 6\text{H}_2\text{O}$, Showa Chemical Co. Ltd., Tokyo, Japan), and then this was stirred at 200 rpm for 6 h. The mixture (Ni^{2+} adsorbed CNT; CNT- Ni^{ads}) contained 0.128 mmoles (7.5 mg) of Ni metal ions in a metal loading of Ni/CNT of 30 wt.%. After stirring, 5 mL of a water solution with 0.0386 g NaBH_4 (99%, Sigma-Aldrich, St. Louis, MO, USA) was added (step 2) to samples prepared in the first step and stirred at 200 rpm for 10 s. After that, metastable Ni metal nanoparticles (NPs) were formed (Ni/CNT sample). In step 3, 1.28 g of a Pt precursor solution, 0.128 mmoles Pt metal ions (i.e., 0.1 M), was added to the Ni/CNT sample, and then a thin layer of Pt crystals on the surface of nickel NPs (namely Ni@Pt-1010) was formed. In this step, Pt ions could be reduced by an excessive amount of NaBH_4 added in step 2 and deposited on the Ni surfaces. According to different Pt/Ni molar ratios, Pt shells with different thicknesses were obtained. The Pt precursor solution was prepared by diluting ~1.0 g $\text{H}_2\text{PtCl}_6 \cdot 6\text{H}_2\text{O}$ (99%, Sigma-Aldrich Co., Burlington, MA, USA) to 18.36 g with distilled water. In the remainder of this article, Ni@Pt NCs with Pt/Ni atomic ratios of 1.0 and 0.4 are called Ni@Pt-1010 and Ni@Pt-1004, respectively.



Scheme 1. Crystal growth pathways of Au-decorated Ni@Pt (NPA) nanocatalysts (NCs) with variable Pt/Ni ratios. Among them, pathways A, B, and C respectively correspond to chemisorption of Au^{3+} , galvanic replacement of Au^{3+} with Ni^0 , and redeposition of Ni^{2+} on the Ni@Pt surface. Steps i and ii refer to the respective addition of 2.0 and 9.0 wt.% of Au^{3+} to the reaction system.

2.2. Synthesis of Atomic Au Cluster-Decorated Ni Core-Pt Shell (NPA) NCs

A precursor solution of Au was prepared by diluting ~13.3 mg $\text{HAuCl}_4 \cdot 3\text{H}_2\text{O}$ (99.0%, Sigma-Aldrich Co., Burlington, MA, USA) to 500 mg with distilled water. After 20 min, once the reaction was complete in step 3, an appropriate amount of the prepared Au solution was added to a solution to make Au/Pt atomic ratios of 0.06 and 0.2. During this stage, Au clusters formed and were intercalated in the Pt shell region through a galvanic replacement reaction of Au^{3+} with Pt, and then with the reducing agent, NaBH_4 , these metal ions decreased. Finally, products of atomic Au cluster-decorated Ni@Pt (NPA) NCs were obtained. The resulting precipitate was washed several times with acetone, centrifuged, and then dried at 70 °C. In the remainder of this article, Au cluster-deposited Ni@Pt-1004 NCs are called NPA-1004006 and NPA-100402 for 2 and 9 wt.% Au loadings, respectively. Furthermore, Au cluster-deposited Ni@Pt-1010 NCs were named NPA-1010006 and NPA-101002 for 2 and 9 wt.% Au loadings, respectively.

2.3. Physical Characterizations of NPA NCs

Physical properties of the prepared NCs were determined by cross-referencing results of microscopic and X-ray spectroscopic techniques. High-resolution transmission electron microscopic (HRTEM) characterizations were carried out at the electron microscopy center of National Sun Yat-Sen University (Kaohsiung, Taiwan). X-ray photoemission spectroscopy (XPS) of the experimental NCs was executed at beamlines BL-24A1 of the National Synchrotron Radiation Research Center (NSRRC) (Hsinchu, Taiwan). X-ray diffraction (XRD) patterns were collected at an incident X-ray wavelength of 1.5406 Å (8.04 keV) at Taiwan beamline of BL-12B2 in Spring-8 (Hyogo, Japan).

2.4. Preparation of the Electrode and the Method for the ORR Activity Experiment

Catalyst ink for the ORR experiment was made by dispersing 5.0 mg of catalyst powder in a solution consisting of 1.0 mL isopropanol and 50 μL Nafion-117 (99%, Sigma-Aldrich Co., Burlington, MA, USA). This mixture was subjected to ultrasonication for 30 min prior to the ORR test. To conduct the ORR test, 10.0 μL of catalyst ink was drop-cast and air-dried on a glossy carbon rotating disk electrode (RDE) (0.196 cm^2 in area) as the working electrode. The Hg/HgCl₂ (with the voltage calibrated to 0.242 V, to align with that of the reference hydrogen electrode (RHE)) electrode saturated in a KCl aqueous solution and a platinum wire were respectively used as the reference and counter electrodes. The ECSAs of the experimental catalysts were calculated by acquiring the coulombic charge for reduction of the monolayer Pt oxide after integration and double-layer correction using the following equation:

$$ECSA = \frac{Q_{Pt}}{Q_{ref} \times m}; \quad (1)$$

where Q_{ref} is the charge required for reduction of the monolayer oxide from the bright Pt surface (i.e., 0.405 mC cm^{-2}), m is the metal loading, and Q_{Pt} is the charge required for oxygen desorption, as calculated by following equation:

$$Q_{Pt} = \frac{1}{\nu} \int (I - I_d) dE. \quad (2)$$

Here, ν is the scan rate for the cyclic voltammetric (CV) analysis, and integral parts refer to the area under the Pt oxide reduction peak on CV curves. The kinetic current density (J_K) and number of electrons transferred in ORRs were calculated based on the following equations:

$$\frac{1}{J} = \frac{1}{J_K} + \frac{1}{J_L} = \frac{1}{J_K} + \frac{1}{B\omega^{0.5}} \text{ and} \quad (3)$$

$$B = 0.62nFC_{O_2}D_{O_2}^{\frac{2}{3}}\nu^{-\frac{1}{6}}; \quad (4)$$

where J , J_K , and J_L are the experimentally measured, mass transport free kinetic, and diffusion-limited current densities, respectively. ω is the angular velocity of the electrode, n is the transferred electron number, F is the Faraday constant, C_{O_2} is the bulk concentration of O_2 , D_{O_2} is the diffusion coefficient,

and ν is the kinematic viscosity of the electrolyte. For each NC, the MA and SA were respectively obtained when J_K was normalized to the Pt loading and ECSA. Details of the procedure for the ORR mass activity calculation are given in electronic supplementary information (ESI).

2.5. Electrochemical Measurements

Electrochemical measurements were carried out at room temperature (25 ± 1 °C) using a potentiostat (CH Instruments Model 600B, CHI 600B; Hsinchu, Taiwan) equipped with a three-electrode. Cyclic voltammetry (CV) and linear sweep voltammetry (LSV) data were measured at voltage scan rates of 0.02 and 0.001 V s⁻¹, potential ranges of 0.1~1.3 V (vs. the RHE.) and 0.4~1.1 V (vs. the RHE) in an aqueous alkaline electrolyte solution of 0.1 M KOH (pH 13). A rotation rate of 400~3600 rpm was used for LSV. N₂ and O₂ atmospheres were used for CV and LSV, respectively.

3. Results and Discussion

The particle shape, near-surface configurations, and crystal structure of the experimental NCs were determined using HRTEM analyses. As shown in Figure 1a, Ni@Pt-1004 NPs (Pt/Ni ratio = 0.4) had ordered atomic arrangements at (111) facets exposing the surface (denoted by red arrows). The presence of a clear twin boundary (denoted by a white line) suggested the formation of semi-coherent interfaces. The interplanar spacing of the (111) facet was determined to be 2.239 Å. This value is about 1.25% smaller than that of the Pt-CNT (2.267 Å) indicating the presence of compressive lattice strain in the shell region. With an average particle size of 2.64 nm in (111) facets (determined by an XRD analysis described in a later section), the surface-to-bulk ratio was estimated to be ~50%. In this event, considering the ideal case of conformal deposition of Pt atoms by chemisorption and reduction, formation of an incomplete Pt shell over the Ni-core crystal was expected. In contrast, Ni@Pt-1010 NPs (Figure 1d) had grown into isotropic spheres, which comprised a complete Pt-shell and Ni core crystal underneath, and this was also confirmed by XPS analyses in a later section. Compared to that of Ni@Pt-1004 NPs, a higher extent of surface defects (denoted by yellow arrows) was observed in Ni@Pt-1010 NPs. The average particle size of Ni@Pt NCs was observed to be around 2~3 nm, which is consistent with XRD findings in a subsequent section.

Shown in Figure 1b, compared to that of Ni@Pt-1004 NPs, the diameter of NPA-1004006 (i.e., Ni@Pt-1004 NC decorated with 2.0 wt.% of Au atoms) nearly doubled by mixing with Au³⁺ ions for 2 min, followed by the addition of a reducing agent (NaBH₄). NPA-1004006 particles grew in a disk-like shape (Figure 1b) with twin boundaries between the NPs. With a nearly identical coherent length to that of Ni@Pt-1004, the large particle was an agglomeration cluster with structural modulations at semi-coherent interfaces between NPs by the galvanic replacement of Au³⁺ to core (Pt/Ni) metals simultaneously with the reduction of residual Pt⁴⁺, Ni²⁺, and Au³⁺ ions by the reducing agents. Such a hypothesis was confirmed by XRD and XPS analyses in later sections. With an incomplete Pt shell structure, certain parts of the NiO_x core were exposed to the liquid environment. In this event, a high content of Ni atoms participated in the galvanic replacement reaction by interacting with Au³⁺ ions. Therefore, Au atoms tended to form metallic clusters between the NPs. As shown in Figure 1c, with a further increase of Au loading to 9 wt.% (NPA-100402), discrete local domains were formed with lattice fringes pointing in different directions (denoted by green arrows). Such a characteristic further revealed severe galvanic replacement of the NiO_x core followed by agglomeration of Ni@Pt NPs by reduction and deposition of residual metal ions in their interfaces. In this event, because of sufficiently high Au loading, the majority of Au atoms were deposited on the top of and between the NPs. Compared to that of Ni@Pt-1004, restructuring of Ni@Pt-1010 by Au³⁺ was insignificant. As shown in Figure 1e,f, particles tended to grow in a core-shell structure with highly ordered atomic arrangements on the surface with increasing Au contents. Such a characteristic was consistently proven by an XRD analysis, which showed that the coherent length of the Pt crystal (111) facet had increased from 2.72 to 3.34 ± 0.1 nm by adding 2.0 wt.% of Au atoms (namely NPA-1010006). Compared to that of NPA-1010006, further increasing Au atoms to 9 wt.% reduced the coherent length to 3.03 ± 0.1 nm, which could be attributed to restructuring between Pt crystals and Au³⁺ ions followed by formation of

Au crystals in the shell region (shown by the presence of a shoulder on the left hand side of the Pt (111) peak). EDX results of NPA-1004006 NC has been shown in Figure S1.

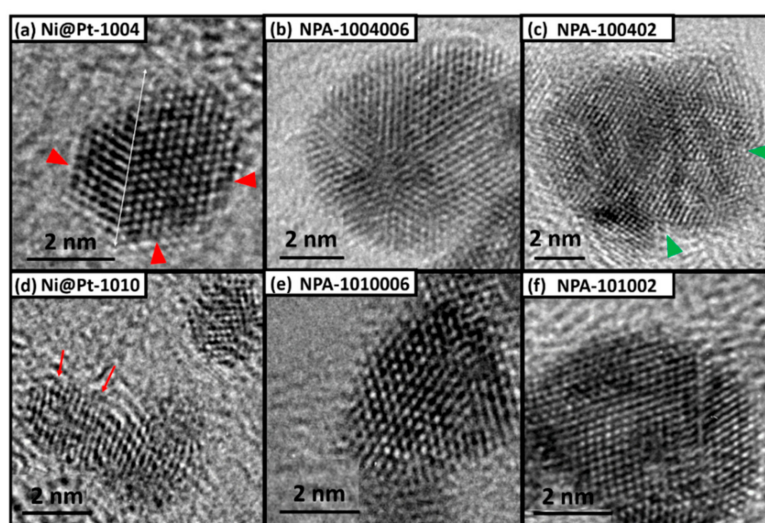


Figure 1. HRTEM images of experimental nanocatalysts (NCs). (a) Ni@Pt-1004 NC with Pt/Ni ratios of 0.4 (b) and 2.0 wt.% Au-cluster-decorated Ni@Pt-1004 NCs (NPA-1004006), (c) 9.0 wt.% Au-cluster-decorated Ni@Pt-1004 NCs (NPA-100402), (d) Ni@Pt-1010 NCs with Pt/Ni ratios of 1.0 (e) and 2.0 wt.% Au cluster-decorated Ni@Pt-1010 NCs (NPA-1010006), and (f) 9.0 wt.% Au cluster-decorated Ni@Pt-1010 NCs (NPA-101002).

Lattice strain, the coherent length (D_{avg}), and the crystallinity of pristine NCs were revealed by XRD analyses. Figure 2 compares XRD patterns of the experimental NCs. Values of the D_{avg} of experimental NCs were calculated from the XRD peak broadening of (111) facets using the Scherrer equation, and their corresponding structural parameters are summarized in Table 1. As indicated in Figure 2, peaks X1 and X2 centered at 40.2° and 46.4° respectively refer to diffraction signals from (111) and (200) facets of metallic-phase Pt nanocrystals in the NCs. In an XRD pattern, the peak width denotes the relative dimension of long-range ordering in specific facets (i.e., the coherent length, D_{avg}) and the ratio of peak intensities between the (111) and (200) facets (i.e., $h(111)/h(200)$), which refers to the extent of preferential crystal growth for samples under investigation. For Ni@Pt NCs (Figure S2), the D_{avg} increased by 0.1 nm, which could be attributed to the formation of thin layers of Pt in the shell region over the Ni core crystal with Pt/Ni ratios of 0.4 (Ni@Pt-1004) and 1.0 (Ni@Pt-1010) (Table S1). A slight shift in diffraction peaks to the low-angle side features lattice expansion by increasing Pt/Ni ratios from 0.4 to 1.0. Meanwhile, the suppression of NiO_x peaks again consistently revealed increased shell coverage with Pt loading. An even closer inspection of D_{avg} values in (111) and (200) facets reveals the morphology of NCs. The Pt-CNT possessed the highest $D(111)/D(200)$ ratio of 1.33 (higher $D(111)$) and thus the largest extent of preferential crystal growth along the (111) facet among the experimental NCs. Such a result rationalizes the intrinsic nature of the atomic arrangement in close-packed facets in Pt metal. For Ni@Pt-1004, compared to that of Pt-CNT, the $D(111)/D(200)$ ratio decreased by 0.22, which could be attributed to the competition of crystal growth between galvanic replacement of Pt^{4+} to Ni atoms in the open-(High-Miller-index facets) and Pt deposition in close-packed facets (111). In this status, a semi-coherent lattice match was found between facets with truncated surfaces, which can be explained by the formation of twin boundaries as revealed on HRTEM images (Figure 1a). For Ni@Pt-1010, high contents of Pt^{4+} ion reduction and deposition on the NC surface induced severe galvanic replacement to the NiO_x core. Such a phenomenon mostly occurred at interfaced corners and edges resulting in a high content of surface truncation in NCs. In this event, NCs tended to form a spherical shape (Figure 1d) due to the strong competition of galvanic replacement to Pt deposition, which was confirmed by a substantially reduced $D(111)/D(200)$ ratio (0.95) compared to that of Pt-CNT.

Table 1. Structural parameters of experimental nanocatalysts (NCs) and control samples as determined by XRD and TEM.

Sample	Pt (111) Facet		Pt (200) facet		Au (111) Facet		Au (200) facet	
	d (Å)	D (nm)	d (Å)	D (nm)	d (Å)	D (nm)	d (Å)	D (nm)
Pt-CNT	2.267	3.52 ± 0.1	1.969	2.63 ± 0.1				
Ni@Pt-1004	2.239	2.64 ± 0.1	1.955	2.38 ± 0.1				
NPA-1004006	2.252	3.03 ± 0.1	1.962	2.50 ± 0.1	2.362	8.24 ± 0.1	2.049	8.09 ± 0.1
NPA-100402	2.266	2.35 ± 0.1	1.965	2.92 ± 0.1	2.352	8.85 ± 0.1	2.043	4.85 ± 0.1
Ni@Pt-1010	2.244	2.72 ± 0.1	1.955	2.86 ± 0.1				
NPA-1010006	2.245	3.34 ± 0.1	1.949	3.01 ± 0.1	2.318	1.75 ± 0.1	2.331	2.63 ± 0.1
NPA-101002	2.254	3.03 ± 0.1	1.960	2.98 ± 0.1	2.046	1.91 ± 0.1	2.046	2.88 ± 0.1

Here “d” and “D” refers to interplanar spacing and average particle size respectively.

After adding different contents of Au to Ni@Pt-1004 NCs (Figure 2a), changes in the lattice strain and crystallinity were obvious due to atomic restructuring. In the case of Ni@Pt-1004 NCs, because of a lower Pt-content (Pt/Ni ratio of 0.4), complete coverage of the Ni-core from Pt atoms was not possible. Thus, with a lesser Au content (NPA-1004006), most of the Au atoms were intercalated with Pt atoms, which aggregated between NCs as revealed by the smeared diffraction peaks across the (111) and (200) facets. Restructuring by formation of Au-rich areas at high-order facets (i.e., (200)) between NCs was significant. These characteristics resulted from the spontaneous trans-metalation between Au³⁺ ions and Ni metal atoms (galvanic replacement) accompanied by redeposition of Ni/Au atoms in shell crystals. Such a phenomenon was consistently proven by the suppressed diffraction signals (peaks M1 and M2) of the Au (111) and (200) facets. Further increasing the Au loading to 9 wt.% (NPA-100402) led to obviously increased diffraction signals for the Au (111) and (200) facets, which revealed the presence of discrete Au clusters (~2 nm) on the surface. At the same time, some of the Au atoms tended to deposit on the shell and core regions. Restructuring of Ni@Pt-1010 by interacting with Au³⁺ ions showed a completely different behavior compared to that of Ni@Pt-1004. As shown in Figure 2b, diffraction peaks X₁ and X₂ were not smeared; on the other hand, they were enhanced by the increasing Au contents from 2.0 to 9.0 wt.%. Such characteristics reveal that the long-range ordering of Ni@Pt NCs was improved by Au decoration. In the absence of diffraction peaks from the Au metal phase and the enhanced Au-4f photoemission peaks (Figure S6, in supplementary information), one can notice that the galvanic replacement of Au³⁺ to the NC surface was suppressed, which suggests conformal deposition of Au atoms in the Pt-rich shell.

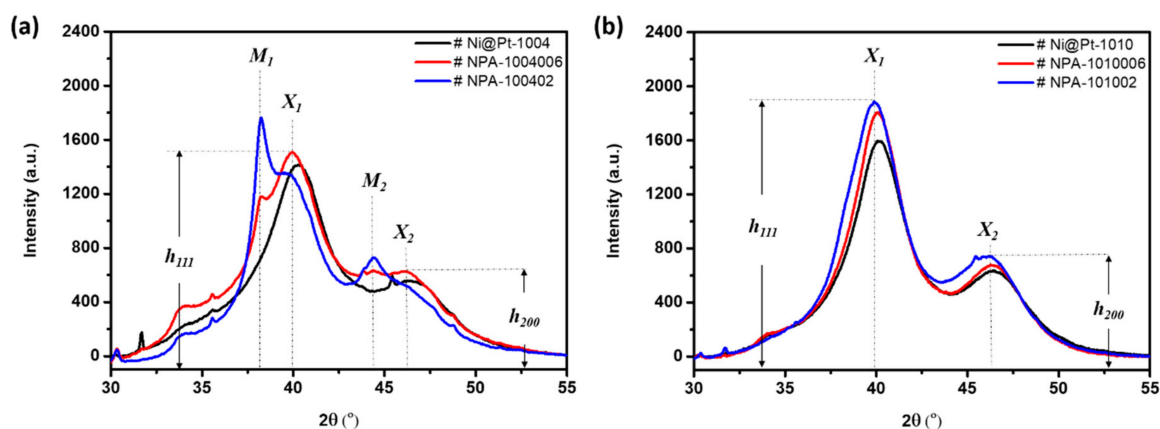


Figure 2. X-ray diffraction patterns of experimental nanocatalysts (NCs) (a) NPA-1004006 and NPA-100402 NCs compared to that of the control sample (Ni@Pt-1004), and (b) NPA-1010006 and NPA-101002 NCs compared to that of the control sample (Ni@Pt-1010). Peaks “X₁” and “X₂” respectively correspond to diffraction signals from the (111) and (200) facets of NCs (Pt). In contrast, peaks “M₁” and “M₂” respectively correspond to diffraction signals from the (111) and (200) facets of NCs (Au).

The XPS analysis was performed in order to investigate the surface chemical composition (1–2 nm from the surface) and binding energy (BE) of elements in experimental NCs. The incident X-ray with an excitation energy of 650 eV corresponding to a probing depth of ~2.6 nm was employed to probe the Pt-4f, Ni-2p, and Au-4f orbitals. Figure 3 reveals the typical fitted XPS spectra in the Pt-4f region of experimental NCs. In the Pt-4f spectrum, doublet peaks at 71 and 74 eV, respectively, emerged as photoelectron emission lines from the Pt-4f_{7/2} and Pt-4f_{5/2} orbitals. The peaks are further deconvoluted to separate the signals from different oxidation states, and corresponding results are given in Table 2. Through an analysis of XPS patterns of Ni@Pt-1004 and Ni@Pt-1010 NCs (Figure 3a,b), it can be seen that most of the Pt was in a zero-valence state (metallic state). In contrast, from the XPS spectra of Ni-2p orbitals (Figure S3), it is clearly evident that Ni is present in an oxidized (NiO_x) form in both Ni@Pt NCs (i.e., Ni@Pt-1004 and Ni@Pt-1010). An even closer inspection of the intensities of the XPS spectra of Ni-2p (Figure S3) revealed that NiO_x signals in Ni@Pt-1010 NCs were very much suppressed compared to those of Ni@Pt-1004 NCs. These spectral characteristics confirmed the core-shell structure of Ni@Pt-1010 NCs comprising a Ni core and Pt in the outermost layer. Meanwhile, the profound intensities of Ni-2p emission peaks in Ni@Pt-1004 NC refer to an incomplete Pt-shell over an underlying Ni-crystal. Those results again confirm prior HRTEM and XRD findings.

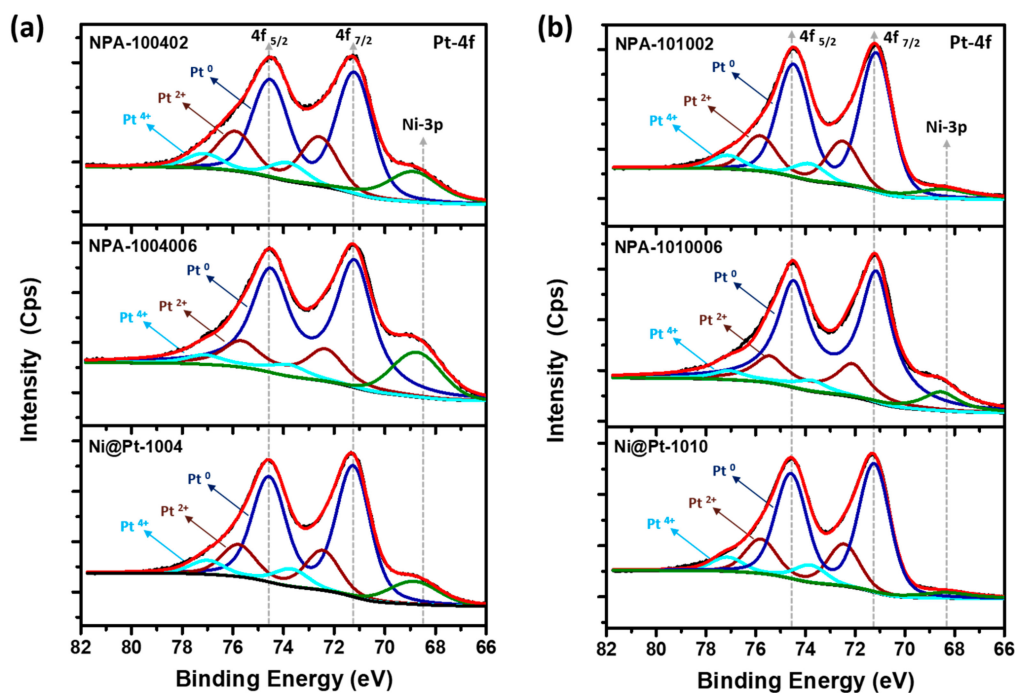


Figure 3. X-ray photoemission spectroscopy of experimental nanocatalysts (NCs). (a) Pt-4f/Ni-3p orbitals of Ni@Pt-1004, NPA-1004006, and NPA-100402. (b) Pt-4f/Ni-3p orbitals of Ni@Pt-1010, NPA-1010006, and NPA-101002.

Table 2. Comparative XPS-determined composition ratios and binding energies of experimental nanocatalysts.

Sample	Binding Energy (eV)			Chemical State Composition (%)		
	Pt ⁰	Pt ²⁺	Pt ⁴⁺	Pt ⁰	Pt ²⁺	Pt ⁴⁺
Ni@Pt-1004	71.24	72.45	73.68	70	21	9
NPA-1004006	71.20	72.34	73.78	74	19	7
NPA-100402	71.20	72.58	73.8	64	26	10
Ni@Pt-1010	71.23	72.45	73.79	68	22	10
NPA-1010006	71.16	72.11	73.74	75	19	6
NPA-101002	71.15	72.5	73.81	70	22	8

For Au-cluster-decorated Ni@Pt-1004 NCs (Figure 3a), significant restructuring of the surface atomic arrangement was observed. NPA-1004006 NCs (2 wt.% Au) exhibited a higher extent of zero-valent Pt (Pt^0) contents on the surface compared to that of NPA-100402 (9 wt.% Au). More evidence of such atomic restructuring came from the XPS analysis of Ni-2p orbitals (Figure S4). Compared to that of Ni@Pt-1004, we observed that the intensity of the Ni-2p emission peak was gradually suppressed with an increasing amount of Au of 2 to 9 wt.%. Intensities of emission peaks in an XPS spectrum are positively related to the electron density in probing orbitals of target atoms. Therefore, the higher intensity found in the curve of NPA-1004006 revealed that its most abundant 2p electrons were Ni atoms, compared to that of NPA-100402 NCs. Similar spectral changes were observed for Au-cluster-decorated Ni@Pt-1010 NCs (Figure 3b). Obtained XPS results were very consistent with former structural characterizations. The difference in binding energy of the $4f_{7/2}$ orbital of zero-valent Pt (Pt^0) was not obvious in the experimental NCs, revealing that electron relocation between Pt and neighboring atoms was nearly absent. For comparison XPS spectra of Ni@Pt-1010, NPA-1010006 and NPA-101002 at Ni-2p orbitals are compared in Figure S5.

XPS spectra of experimental samples of Au-4f orbitals are compared in Figure S6. Accordingly, intensities of Au- $4f_{5/2}$ and Au- $4f_{7/2}$ peaks increased with Au contents from 2 (NPA-1004006) to 9 wt.% (NPA-100402). Such a phenomenon shows the increasing exposure of Au with loading, which again consistently proves the formation of Au clusters in Ni@Pt NCs with an incomplete shell structure. In the case of Ni@Pt-1010, when the Au loading was 2.0 wt.%, the doublet peaks in the Au-4f orbital were insignificant. Such a result can be complementarily explained by the crystal structure parameters. As indicated in Figure 2b, a significant improvement in Pt crystallinity was found, and diffraction peak shifts were absent when decorated with 2 wt.% of Au atoms on the Ni@Pt surface. These features indicate the formation of atomic Au clusters on the NiO_x @Pt surface. Therefore, the presence of weak emission peaks suggests a discrete and smeared 4f orbital of Au atomic clusters that were finely dispersed in surface defect sites of NiO_x @Pt NCs. By increasing Au to 9 wt.%, pronounced Au-4f peaks rationalized the formation of Au sub-nano- or nanoclusters, as revealed by presence of a diffraction shoulder on the low-angle side of X1 (111) and a pronounced intensity in X2 (200) peaks.

By cross-referencing results of the physical characterization, the effects of Au^{3+} loading and Pt contents on the evolution of atomic structures of Ni@Pt NCs was systematically determined, and corresponding structural models are given in Scheme 1—where the upper and lower layers respectively present changes in the atomic structure with increasing Au^{3+} loading for Ni@Pt-1004 and Ni@Pt-1010. Accordingly, a significant galvanic replacement on oxidation followed by dissolution of Ni^0 to Ni^{2+} appeared by interacting Ni@Pt-1004 with 2 wt.% of Au^{3+} (step i in the upper layer of Scheme 1) with the reaction of $\text{Au}^{3+} + \text{Ni}^0$ (or Pt^0) $\text{Au}^0 + 3/2\text{Ni}^{2+}$ (or $4/3\text{Pt}^{4+}$), where Au^{3+} has a higher selectivity for Ni^0 than Pt^0 due to the larger electronegativity difference. In this event, Au atoms tended to penetrate the core region, thus resulting in the coexistence of nanosized Au and Pt clusters in NiO_x @Pt NPs. By increasing the loading to 9 wt.%, galvanic replacement between Au^{3+} ion and core crystals was further enhanced, which caused the severe interparticle agglomeration by dissolution of core metal atoms accompanied by the rapid redeposition of residual metal ions between interfaces (i.e., regions a, b, and c in step ii of the upper layer of Scheme 1) of the NPs. Compared to those of Ni@Pt-1004, the effects of Au^{3+} loading on the structural evolution were suppressed by the high contents of the Pt shell structure in Ni@Pt-1010. As shown in the bottom layer of Scheme 1, Au^{3+} tended to be adsorbed and was reduced by NaBH_4 to form atomic clusters on the NP surface with a loading of 2.0 wt.% (NPA-1010006). By increasing the loading to 9.0 wt.%, the Au^{3+} ions tended to form homoatomic bonds and thus grew into sub-nanometer crystals on the NPA-101002 surface (step ii in the bottom layer of Scheme 1). These atomic structural arrangements provide direct information explaining ORR activities of the experimental NCs.

In heterogeneous catalysts, dissociation of chemisorbed oxygen molecules (i.e., the oxygen adsorption strength) is a cardinal performance-determining factor in ORRs. Lowering the oxygen adsorption energy reduces the applied energy for initiating ORRs at reaction sites and relocating them

to neighboring atoms. In this way, the reaction kinetics and ORR activities of NCs can be substantially improved. In this study, the surface composition design of catalysts within the sub-nano scale played a key role in ORR performances of the NCs. By cross-referencing physical inspection results (the upper layer of Scheme 1), the surface chemical configuration of NiO_x@Pt comprised mixtures of sub-nano Au and Pt clusters in the shell region and Au clusters intercalated with NiO_x in the core when the Pt/Ni ratio was 0.4 and Au was 2.0 wt.%. With an Au content of 9.0 wt.%, severe interparticle agglomeration due to galvanic replacement ($\text{Au}^{3+} + \text{Pt/Ni} \rightarrow \text{Au} + \text{Pt}^{4+}/\text{Ni}^{2+}$) accompanied by Au crystal growth and redeposition of residual metal ions between NCs occurred. All three pathways dramatically reduced the degree of heteroatomic intermixing on the surface among reaction sites; therefore, ORR activities of those NCs were substantially suppressed.

Results of the electrochemical analyses consistently elucidated the above scenarios. Figure 4a compares CV curves of the commercial Johnson Matthey-Pt/C catalyst (Johnson Matthey-Pt/C) with the experimental NCs (i.e., Ni@Pt-1004, NPA-1004006, and NPA-100402). Electrochemical active surface areas (ECSAs) are calculated based on corresponding CV curves using the oxygen desorption peak in the backward potential sweeping curve (detailed ECSA data of various ORR catalysts are listed in electronic supplementary information in Table S2). Three distinctive potential regions are found in a CV curve, including an under-potential deposition of hydrogen (UPD-H) region at $0 < E < 0.4$ V, a double-layer region between 0.4 and 0.6 V, and chemisorption of oxygen species at >0.6 V vs. the RHE because of hydrogen adsorption/desorption, OH⁻ ligand chemisorption, and the formation of alpha Pt oxide ($E_{\text{O}}^{\text{ads}}$; forward scan) as well as a reduction in Pt oxides ($E_{\text{O}}^{\text{des}}$; backward scan). In this way, the position and width of each peak are susceptible to the chemical composition and structure of the NC surface. For the Johnson Matthey-Pt/C, positions of two characteristic peaks (H_1 and H_2) in the forward scan denoted the potential to be applied for dissociation of H⁺ from close-packed (111) and opened (200) facets and the corresponding current, respectively. In contrast, peaks H_1^* and H_2^* respectively refer to current responses of H⁺ adsorption in the (111) and (200) facets. For Ni@Pt-1004, compared to the CV profile of the Johnson Matthey-Pt/C, a downshift of peaks H_1 and H_2 in the forward scan and an upshift of peaks H_1^* and H_2^* in the backward scan refer to a decreased energy barrier for redox desorption/adsorption of H⁺. As consistently shown by XRD observations, a substantially higher intensity of peak H_1 than that of peak H_2 (i.e., weakened H⁺ interactions on (200) facets) revealed preferential crystal growth at (111) facets in all experimental NCs.

Compared to that of the Johnson Matthey-Pt/C, Ni@Pt-1004 showed a higher surface area for H₂ evolution as revealed by the larger area of the UPD_H region. Meanwhile, the broadened and smeared UPD_H peaks revealed a high density of surface defects in Ni@Pt-1004. This statement is consistently illustrated by the pronounced oxygen adsorption peak ($E_{\text{O}}^{\text{ads}}$) with a potential shift by ca. ~ 0.17 V (i.e., easy oxidation of the Ni@Pt-1004 surface) compared to that of the Johnson Matthey-Pt/C. Compared to the CV profile of NCs without Au decoration, a slight amount of Au decoration reduced the surface defect sites of Ni@Pt-1004, as consistently revealed by the significant suppression of the $E_{\text{O}}^{\text{ads}}$ and $E_{\text{O}}^{\text{des}}$ peaks in NPA-1004006. Moreover, the position of the oxide reduction peak ($E_{\text{O}}^{\text{des}}$) was upshifted to high-potential sites at the same time. These two observations integrally bring out the fact that atomic decoration by Au clusters can fix the defect and simultaneously suppress the surface oxidation on the Ni@Pt-1004 surface. In the presence of discrete 4f orbitals in atomic clusters, a strong repulsive force to the chemisorbed O (O^{ads}) was formed at Au atoms. This relocated the O^{ads} to neighboring atoms around the Pt and Au interfaces and thus substantially boosted the ORR kinetic current (J_k) of NPA-1004006 to ~ 75 mA cm⁻² (details discussed below in the LSV analysis, Figure 4c). For NPA-100402, the H⁺ adsorption peak, " H_1^* ", in the backward scan together with a smeared CV profile in forward scan was observed in the UPD_H region. Such a feature can be rationalized by its nanostructure, where the surface of the NC consists of nanosized Au/Pt clusters. Meanwhile, a severe interparticle agglomeration by the strong galvanic replacement accompanied by rapid reduction of residual metal ions was found (Figure 1c, Scheme 1); therefore, the heteroatomic intermix and the amount of reaction sites dramatically decreased. Formation of cluster-in-cluster

structures turned 4f orbitals from a discrete state into a band structure. In this state, both the Au and Pt atoms possessed bulk properties, and consequently the J_k of NPA-100402 was dramatically reduced by 87% (65.62 mA cm^{-2}) to 9.4 mA cm^{-2} (Table S2), compared to that of NPA-1004006. This value was even lower than that of Ni@Pt-1004, indicating that the impact of the heterogeneous interface between nanoclusters on ORR activity was limited.

On the other hand, as shown in Figure 4b, changes in profiles in CV curves were insignificant by decoration with Au atoms on Ni@Pt-1010. In the case of 2.0 wt.% Au decoration, a slight suppression of both E_{O}^{ads} and E_{O}^{des} was found for NPA-1010006 NCs compared to that of Ni@Pt-1010. These characteristics resemble the same redox response to O adsorption and desorption when decorating Au atomic clusters on the Ni@Pt-1004 surface. Increasing the Au content to 9.0 wt.% did not further suppress the redox peaks of O evolutions ($E_{O}^{\text{ads}}/E_{O}^{\text{des}}$); however, they moved in an opposite direction. Due to the strong preference for homoatomic bonding, Au atoms tended to form sub-nano clusters instead of a conformal coating or defect sites on NC Pt surfaces. Those characteristics reduced the heteroatomic intermix and amount of O_2 -splitting sites in NCs. The former suppresses intrinsic activity, and the latter reduces the number of active sites; therefore, the J_k of NPA-101002 was substantially reduced by 70% (to $\sim 22 \text{ mA cm}^{-2}$), compared to that of NPA1010006. Again, given that most of the Au atoms were deposited as sub-nanometer clusters or atomic clusters (shown by absence of an Au diffraction peak in the XRD pattern of Figure 2b), a high J_k ($\sim 22 \text{ mA cm}^{-2}$) was expected.

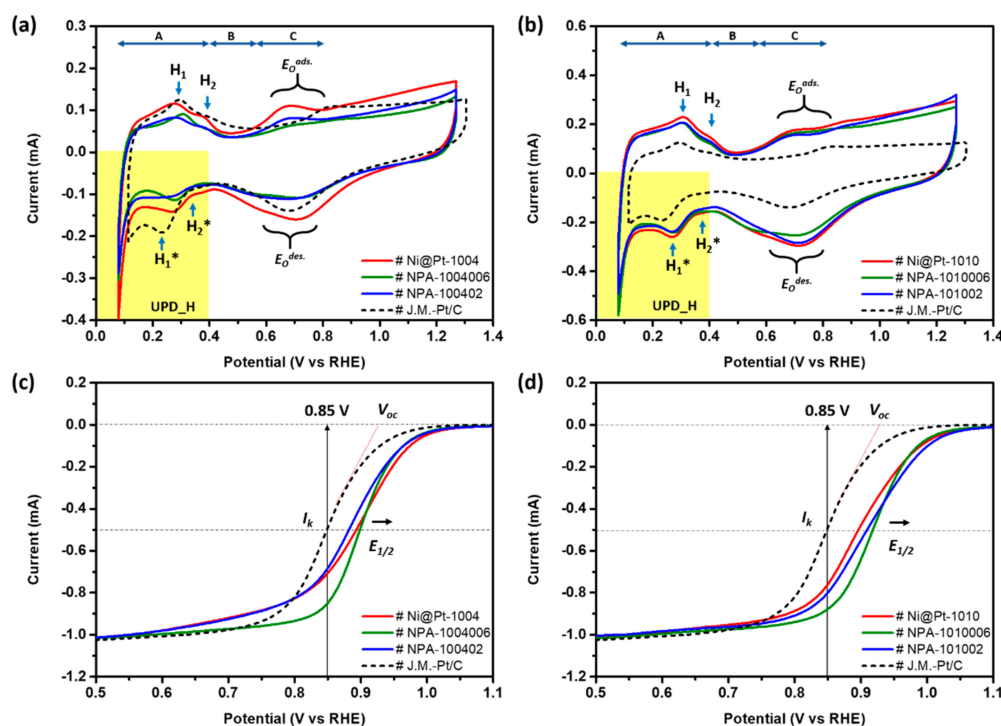


Figure 4. Electrochemical analysis of experimental nanocatalysts (NCs). (a,b) CV and (c,d) LSV curves of experimental NCs compared to a commercial Johnson Matthey-Pt/C NC. Potential sweeping curves were measured at a rotation speed of the electrode of 1600 rpm.

To further rationalize the impacts of Au decoration and Pt contents on ORR activities of Ni@Pt NPs, an LSV analysis was employed. Figure 4c,d demonstrates LSV curves of NPA compared to control samples (Ni@Pt-1004 and Ni@Pt-1010) and the Johnson Matthey-Pt/C, where corresponding electrochemical parameters are summarized in Figure 5, and Tables S2 and S3. As shown in Figure 4c and Table S2, the onset potential (V_{oc} vs. the RHE) of experimental samples followed the trend of the Johnson Matthey-Pt/C (0.910 V) < NPA-1004006 (0.964 V) < NPA-100402 (0.969 V) < Ni@Pt-1004 (0.990 V). Among them, the highest V_{oc} indicates the lowest activation energy for initiating ORRs

on Ni@Pt-1004 surfaces and can be rationalized by a large extent of heteroatomic intermix between Pt and Ni sub-nanoclusters. On such a surface, Pt clusters are in charge of splitting (dissociating) the oxygen molecule (O_2). After O_2 splitting, the two chemisorbed oxygen atoms are relocated to the high-oxygen-affinity Ni atoms for the subsequent reduction reaction. Since the dimensions of Pt clusters are quite small (i.e., the interface ratio between Ni domain is high), a rapid relocation of chemisorbed oxygen atoms to Ni sites is expected; therefore, the J_k of Ni@Pt-1004 doubled compared to that of the Johnson Matthey-Pt/C. By decorating with 2.0 wt.% Au atoms on Ni@Pt-1004, the atomic Au clusters reduced surface defects of the Pt shell and covered the Ni core crystal. In this event, activation energy for O_2 splitting increased, which reduced the intrinsic activities of surface sites and thus the V_{oc} by 0.026 V. Such a phenomenon would seemingly suppress the activity of surface sites on the NC surface; however, it actually went the opposite way. As revealed by results of physical structural inspections, decoration with a slight amount of Au atoms (2.0 wt.%) resulted in a surface structure comprising combinations of Au, Pt, and Ni sub-nanoclusters on the NC surface. The presence of sub-nano or atomic Au clusters in defect sites protected the NC surface from oxidation (shown by the suppressed $E_{O^{ads}}$ peak in the CV curve). In this event, relocation of the O^{ads} was dramatically facilitated, resulting in a quantum leap of J_k by 6.7-fold compared to that of NCs without Au decoration (i.e., Ni@Pt-1004). By increasing Au to 9.0 wt.%, compared to that of NPA-1004006, the J_k of NPA-100402 substantially decreased by ~87% to 9.4 mA cm^{-2} . This value was almost the same as that of Ni@Pt-1004, indicating that all reaction sites (Pt, Au, and Ni) possessed metallic properties of NPs (bulk) without facilitation of heteroatomic intermixing or ligand effects in ORRs. Meanwhile, as shown in Figure 4c, similar slopes of diffusion ($V < 0.8 \text{ V}$ vs. the RHE) and kinetic limit ($V > 0.8 \text{ V}$ vs. the RHE) current regions indicated that the redox responses of Ni@Pt-1004 were not greatly influenced by a high Au loading. Such electrochemical properties are understandable due to the fact that Au atoms tend to form large nanocrystals by homogeneous crystal growth on the surface and galvanic replacement in the core region of Ni@Pt NCs. Compared to those of Ni@Pt-1004, Au decoration showed similar effects on ORR activity of Ni@Pt NCs with a conformal Pt shell (Ni@Pt-1010). Figure 4d compares LSV curves of experimental NCs (NPA-1010006 and NPA-101002) with those of the control sample (Ni@Pt-1010) and the Johnson Matthey-Pt/C; corresponding electrochemical properties are summarized in Table S3. Accordingly, V_{oc} and $E_{1/2}$ followed the same trend as that of Ni@Pt-1004 with increasing Au contents from 2.0 to 9.0 wt.%. The same scenario to NPA NCs with low Pt contents held for NPA-1010006, except that Au atoms did not penetrate into the core region to form nanosized clusters, therefore NPA-101002 retained a high J_k value (21.99 mA cm^{-2}) in ORRs.

Surface activities (SAs) of electrocatalysts in ORRs are calculated by normalizing the J_k to the ECSA of the oxygen desorption region in the CV curve. These values are an important index for the average intrinsic activity of reaction sites on NC surfaces. As shown in Table S2, the ECSA was $81.2 \text{ cm}^2 \text{ mg}^{-1}$ for Ni@Pt-1004 and decreased to $50.0 \text{ cm}^2 \text{ mg}^{-1}$ by decorating with 2.0 wt.% Au atoms, again proving that Au atoms tended to reside in defect sites of the Pt shell. Further increasing the Au content to 9.0 wt.% did not affect the ECSA value. This result, consistent with that proven by the XRD analysis, suggests that Au atoms tended to grow in homoatomic nanocrystals instead of capping on the Pt shell surface. Accordingly, SAs were 13.89 mA cm^{-2} for NPA-1004006 and 1.83 mA cm^{-2} for NPA-100402. With similar ESCAs, the significantly enhanced SA elucidates conformation of the substantially improved intrinsic ORR activity by the presence of atomic/sub-nano Au clusters simultaneously with Pt and Ni nanoclusters on the NPA-1004006 surface. For Ni@Pt with a conformal Pt shell, Au decoration mainly occurred on the NPA-1010006 surface, as indicated by a reduction in the ECSA ($64.4 \text{ cm}^2 \text{ mg}^{-1}$) by 11.9% compared to that of Ni@Pt-1010 ($73.1 \text{ cm}^2 \text{ mg}^{-1}$). Compared to that of NPA-1010006, the ESCA increased by 11.3% when decorated with 9.0 wt.% of Au on the Ni@Pt-1010 surface, which can be attributed to the formation of sub-nano Au clusters on the NC surface. In this event, SAs were 5.64 mA cm^{-2} for NPA-1010006 and 1.61 mA cm^{-2} for NPA-101002. Compared to those of NPA with Pt/Ni = 0.4, the substantially suppressed SA reveals the truth that the combination

of atomic Au/Pt clusters with Ni atoms in neighboring sites can support exceptional reaction kinetics of ORRs (i.e., J_k and SA).

Mass activity (MA) refers to the current density per unit weight of active sites and is calculated by normalizing the residual current at 0.85 V vs. the RHE with respect to the loading amount of metal Pt in NCs. As illustrated in Figure 5a, the MA of Ni@Pt was slightly improved by 26% compared that of the Johnson Matthey-Pt/C. By adding 2.0 wt.% Au atoms on the surface, the MA of NPA-1004006 substantially improved by 7.1-fold compared to that of Ni@Pt-1004. With a slight increment of noble metal loading, such a dramatic improvement in the MA depicts the truth for boosting the activity of NCs by syngeneic collaboration between sub-nano Au, Pt, and Ni domains in the reaction pathways in ORRs. Such a scenario was further confirmed by the MA of NPA-100402. In this NC, the MA was significantly reduced by 87% compared to that of NPA-1004006. Given that the difference in noble metal loading was small (7.0 wt.%), the dramatic difference in the MA again proves changes in intrinsic activities instead of mass differences. The same phenomenon exists in changes of the MA with respect to Au loading in Ni@Pt-1010 again complementarily proves the synergetic effects on ORR activities of NCs. Electrochemical results of control samples with commercial catalyst has been compared in Figure S7 and corresponding parameters has been summarized in Table S4.

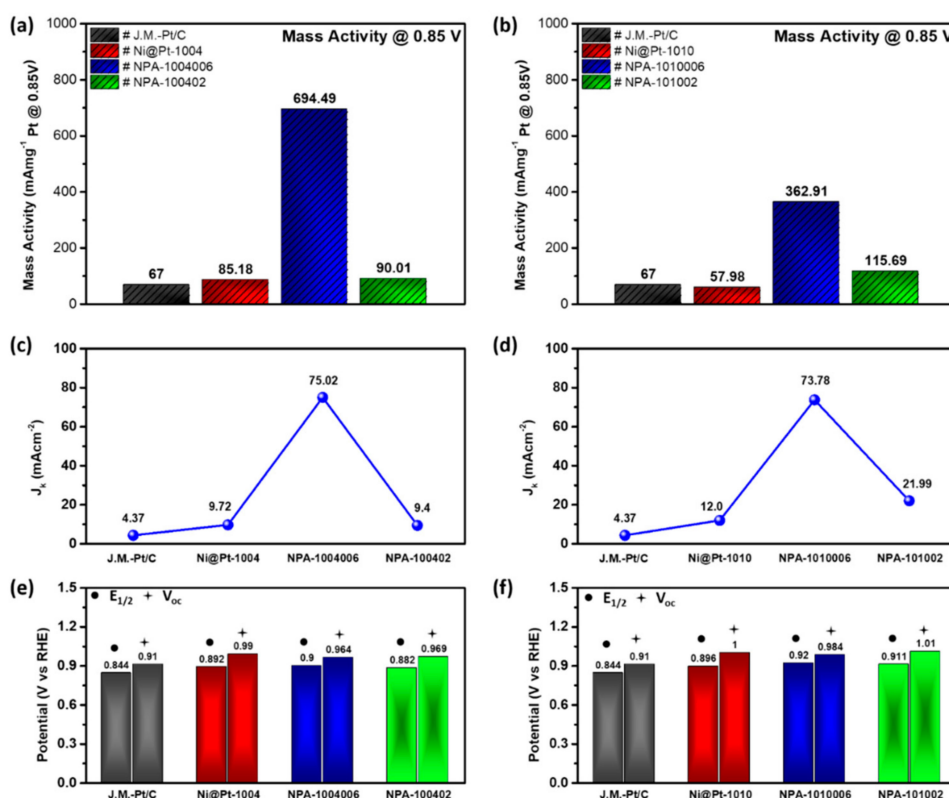


Figure 5. Electrochemical results of experimental nanocatalysts (NCs). (a,b) Oxygen reduction reaction (ORR) mass activity of NCs compared to the commercial Johnson Matthey-Pt/C at 0.85 V (vs. the reference hydrogen electrode (RHE)). (c,d) Kinetic current density of the experimental NCs and Johnson Matthey-Pt/C at 0.85 V (vs. the RHE). (e,f) Onset potential and half-wave potential of the experimental NCs and Johnson Matthey-Pt/C.

4. Conclusions

CNT-supported NCs with a Ni/NiO_x base and an Au cluster-modified Pt-shell were synthesized via self-aligned wet-chemical processes with variable shell thicknesses (Pt/Ni ratios of 0.4 and 1.0) decorated with different contents of Au atoms (2 and 9 wt.%). Results of physical structural characterizations combined with electrochemical analyses proved that surface coverage of the Pt-shell along with depth

and distribution of Au clusters significantly affected inner structural configurations and thus the ORR activities of bimetallic Ni@Pt NCs. For Ni@Pt-1004 NCs, because a lower Pt-content and lower surface coverage were adopted, Au atoms tended to form sub-nanoclusters accompanied by Pt and Ni on the NC surface at a loading of 2.0 wt.%. Such an NC exhibited the highest J_k (75.02 mA cm⁻²), SA (13.89 mA cm⁻²), and MA (694.49 mA mg_{Pt}⁻¹) among the experimental NCs due to the synergetic collaboration between oxygen-inert and -affinity sites on the surface. When increasing the loading to 9.0 wt.%, Au atoms tended to penetrate into the core region and grow into homoatomic clusters on the NC surface. Both characteristics reduced the heteroatomic intermix and surface ratio, and therefore, turned the redox properties of NCs into a bulk nanocrystal state. For the case of Ni@Pt with a conformal shell, Au atoms tended to form atomic clusters on the NC surface which exhibited a J_k of 73.78 mA cm⁻² corresponding to an MA of 362.9 mA mg_{Pt}⁻¹ and SA of 5.64 mA cm⁻². Compared to those with low Pt contents, the lower electrochemical performances of NPA with a Pt/Ni ratio of 1.0 consistently explained the local syngeneic effects on the NC surface. In brief, robust methods to synthesize bimetallic NCs with different extents of surface decoration were developed in this study. We demonstrated that such processes can be adopted to control the identity and local structural disorder on NC surfaces. By proper control of the surface decoration loading, the ORR performance of NiO@Pt catalysts was improved by 7.1-fold in the optimal case. These results elucidate a new prospect of heterogeneous catalyst design. It realizes a compact co-catalyst with different sub-nanometer components collaborating together to share intermediate steps in redox reactions and thus enabling facilitation of the activity of electrocatalysts.

Supplementary Materials: The following are available online at <http://www.mdpi.com/2079-4991/9/7/1003/s1>. Figure S1: TEM images of NPA-1004006 NC. The EDX results are measured in the region marked by pink square. Figure S2: XRD patterns of Ni@Pt-1004 and Ni@Pt-1010 experimental NCs. Figure S3: Comparative x-ray photoemission spectroscopy of Ni@Pt-1004 and Ni@Pt-1010 NCs at Ni-2p orbitals. Figure S4: X-ray photoemission spectroscopy of Ni@Pt-1004, NPA-1004006 and NPA-100402 NCs at Ni-2p orbitals. Figure S5: X-ray photoemission spectroscopy of Ni@Pt-1010, NPA-1010006 and NPA-101002 NCs at Ni-2p orbitals. Figure S6: X-ray photoemission spectroscopy of experimental NCs. (a) Au-4f orbitals of NPA-1004006 and NPA-100402. (b) Au-4f orbitals of NPA-1010006 and NPA-101002. Figure S7: Electrochemical analysis of experimental NCs. (a) CV and (2) LSV curves of Ni@Pt-1004 and Ni@Pt-1010 experimental NCs compared with commercial J.M.-Pt/C nanocatalysts. Table S1: XRD and TEM determined structural parameters of control samples. Table S2: Electrochemical parameters of experimental NCs with Pt/Ni = 0.4. Table S3: Electrochemical parameters of experimental NCs with Pt/Ni = 1.0. Table S4: Electrochemical parameters of control samples.

Author Contributions: T.Y.C. conceived the experiments and designed the synthetic procedures of the ternary nanocatalyst. Y.C.L., Y.J.F., C.H.L., and Y.W.Y. Prepared various catalyst samples and performed the electrochemical measurements. All authors analyzed the experimental data. D.B, Y.T.Y, and T.Y.C. wrote the manuscript and prepared the figures. All authors participated in discussions and knew implications of the work.

Funding: This research received no external funding.

Acknowledgments: The authors thank the staff of the National Synchrotron Radiation Research Center (NSRRC), Hsinchu, Taiwan and Spring-8, Japan for helping with various synchrotron-based measurements and XRD analyses. T.-Y. Chen acknowledges the funding support from National Tsing Hua University, Taiwan (N103K30211 and 103N1200K3) and the Ministry of Science and Technology, Taiwan (MOST 106-2112-M-007-016-MY3 and MOST 105-3113-E-006-019-CC2).

Conflicts of Interest: The authors declare no conflict of interest.

References

1. Das, V.; Padmanaban, S.; Venkitesamy, K.; Selvamuthukumar, R.; Blaabjerg, F.; Siano, P. Recent advances and challenges of fuel cell based power system architectures and control—A review. *Renew. Sustain. Energy Rev.* **2017**, *73*, 10–18. [[CrossRef](#)]
2. Hansen, J.; Sato, M.; Ruedy, R.; Kharecha, P.; Lacis, A.; Miller, R.; Nazarenko, L.; Lo, K.; Schmidt, G.A.; Russell, G.; et al. Dangerous human-made interference with climate: A GISS modelE study. *Atmos. Chem. Phys.* **2007**, *7*, 2287–2312. [[CrossRef](#)]
3. Holton, O.T.; Stevenson, J.W. The Role of Platinum in Proton Exchange Membrane Fuel Cells. *Platin. Met. Rev.* **2013**, *57*, 259–271. [[CrossRef](#)]

4. Sasaki, K.; Naohara, H.; Cai, Y.; Choi, Y.M.; Liu, P.; Vukmirovic, M.B.; Wang, J.X.; Adzic, R.R. Core-Protected Platinum Monolayer Shell High-Stability Electrocatalysts for Fuel-Cell Cathodes. *Angew. Chem. Int. Ed.* **2010**, *49*, 8602–8607. [[CrossRef](#)] [[PubMed](#)]
5. Larminie, J.; Dicks, A. *Fuel Cell Systems Explained*, 2nd ed.; John Wiley & Sons Ltd.: Chichester, UK, 2003; pp. 45–66.
6. Vielstich, W.; Lamm, A.; Gasteiger, H.A. *Handbook of Fuel Cells: Fundamentals, Technology, and Applications*; John Wiley & Sons: Hoboken, NJ, USA, 2009; Volume 5.
7. Hernandez-Fernandez, P.; Masini, F.; McCarthy, D.N.; Strebel, C.E.; Friebel, D.; Malacrida, P.; Nierhoff, A.; Bodin, A.; Wise, A.M.; Nielsen, J.H.; et al. Mass-selected of Pt_xY as model catalysts for oxygen electroreduction. *Nat. Chem.* **2014**, *6*, 732–738. [[CrossRef](#)]
8. Mench, M.M.; Kumbar, E.C.; Veziroglu, T.N. *Polymer Electrolyte Fuel Cell Degradation*; Academic Press Elsevier: Waltham, MA, USA, 2012.
9. Zhang, S.; Yuan, X.; Hin, J.N.C.; Wang, H.; Friedrich, K.A.; Schulze, M. A review of platinum-based catalyst layer degradation in proton exchange membrane fuel cells. *J. Power Sources* **2009**, *194*, 588–600. [[CrossRef](#)]
10. Huang, X.; Zhao, Z.; Cao, L.; Chen, Y.; Zhu, E.; Lin, Z.; Li, M.; Yan, A.; Zettl, A.; Wang, Y.M.; et al. High-performance transition metal-doped Pt₃Ni octahedra for oxygen reduction reaction. *Science* **2015**, *348*, 1230. [[CrossRef](#)] [[PubMed](#)]
11. Stamenkovic, V.R.; Fowler, B.; Mun, B.S.; Wang, G.; Ross, P.N.; Lucas, C.A.; Marković, N.M. Improved Oxygen Reduction Activity on Pt₃Ni(111) via Increased Surface Site Availability. *Science* **2007**, *315*, 493. [[CrossRef](#)]
12. Dong, Y.; Zhou, Y.-W.; Wang, M.-Z.; Zheng, S.-L.; Jiang, K.; Cai, W.-B. Facile Aqueous Phase Synthesis of Carbon Supported B-doped Pt₃Ni Nanocatalyst for Efficient Oxygen Reduction Reaction. *Electrochim. Acta* **2017**, *246*, 242–250. [[CrossRef](#)]
13. Jiang, J.; Gao, H.; Lu, S.; Zhang, X.; Wang, C.-Y.; Wang, W.-K.; Yu, H.-Q. Ni–Pd core–shell nanoparticles with Pt-like oxygen reduction electrocatalytic performance in both acidic and alkaline electrolytes. *J. Mater. Chem. A* **2017**, *5*, 9233–9240. [[CrossRef](#)]
14. Luo, L.; Zhu, F.; Tian, R.; Li, L.; Shen, S.; Yan, X.; Zhang, J. Composition-Graded Pd_xNi_{1-x} Nanospheres with Pt Monolayer Shells as High-Performance Electrocatalysts for Oxygen Reduction Reaction. *ACS Catal.* **2017**, *7*, 5420–5430. [[CrossRef](#)]
15. Strasser, P.; Kühn, S. Dealloyed Pt-based core-shell oxygen reduction electrocatalysts. *Nano Energy* **2016**, *29*, 166–177. [[CrossRef](#)]
16. Lim, B.; Jiang, M.; Camargo, P.H.C.; Cho, E.C.; Tao, J.; Lu, X.; Zhu, Y.; Xia, Y. Pd-Pt Bimetallic Nanodendrites with High Activity for Oxygen Reduction. *Science* **2009**, *324*, 1302. [[CrossRef](#)] [[PubMed](#)]
17. Li, M.; Zhao, Z.; Cheng, T.; Fortunelli, A.; Chen, C.Y.; Yu, R.; Zhang, Q.; Gu, L.; Merinov, B.V.; Lin, Z.; et al. Ultrafine Jagged Platinum Nanowires Enable Ultrahigh Mass Activity for the Oxygen Reduction Reaction. *Science* **2016**, *354*, 1414–1419. [[CrossRef](#)] [[PubMed](#)]
18. Choi, E.Y.; Kim, C.K. Fabrication of nitrogen-doped nano-onions and their electrocatalytic activity toward the oxygen reduction reaction. *Sci. Rep.* **2017**, *7*, 4178. [[CrossRef](#)] [[PubMed](#)]
19. Nesselberger, M.; Ashton, S.; Meier, J.C.; Katsounaros, I.; Mayrhofer, K.J.J.; Arenz, M. The Particle Size Effect on the Oxygen Reduction Reaction Activity of Pt Catalysts: Influence of Electrolyte and Relation to Single Crystal Models. *J. Am. Chem. Soc.* **2011**, *133*, 17428–17433. [[CrossRef](#)] [[PubMed](#)]
20. Shao, M.; Chang, Q.; Dodelet, J.-P.; Chenitz, R. Recent Advances in Electrocatalysts for Oxygen Reduction Reaction. *Chem. Rev.* **2016**, *116*, 3594–3657. [[CrossRef](#)]
21. Wang, Y.-J.; Zhao, N.; Fang, B.; Li, H.; Bi, X.T.; Wang, H. Carbon-Supported Pt-Based Alloy Electrocatalysts for the Oxygen Reduction Reaction in Polymer Electrolyte Membrane Fuel Cells: Particle Size, Shape, and Composition Manipulation and Their Impact to Activity. *Chem. Rev.* **2015**, *115*, 3433–3467. [[CrossRef](#)]
22. Park, S.A.; Lee, E.K.; Song, H.; Kim, Y.T. Bifunctional enhancement of oxygen reduction reaction activity on Ag catalysts due to water activation on LaMnO₃ supports in alkaline media. *Sci. Rep.* **2015**, *5*, 13552. [[CrossRef](#)]
23. Bligaard, T.; Nørskov, J.K. Ligand effects in heterogeneous catalysis and electrochemistry. *Electrochim. Acta* **2007**, *52*, 5512–5516. [[CrossRef](#)]
24. Gauthier, Y.; Baudouin, R.; Joly, Y.; Rundgren, J.; Bertolini, J.C.; Massardier, J. Pt_xNi_{1-x}(111) alloy surfaces: Structure and composition in relation to some catalytic properties. *Surf. Sci.* **1985**, *162*, 342–347. [[CrossRef](#)]

25. Greeley, J.; Nørskov, J.K.; Mavrikakis, M. Electronic structure and catalysis on metal surfaces. *Annu. Rev. Phys. Chem.* **2002**, *53*, 319–348. [[CrossRef](#)] [[PubMed](#)]
26. Stamenkovic, V.; Mun, B.S.; Mayrhofer, K.J.J.; Ross, P.N.; Markovic, N.M.; Rossmeisl, J.; Greeley, J.; Nørskov, J.K. Changing the Activity of Electrocatalysts for Oxygen Reduction by Tuning the Surface Electronic Structure. *Angew. Chem. Int. Ed.* **2006**, *45*, 2897–2901. [[CrossRef](#)] [[PubMed](#)]
27. Paffett, M.T.; Daube, K.A.; Gottesfeld, S.; Campbell, C.T. Electrochemical and surface science investigations of PtCr alloy electrodes. *J. Electroanal. Chem. Interfac. Electrochem.* **1987**, *220*, 269–285. [[CrossRef](#)]
28. Hammer, B.; Nørskov, J.K. Electronic factors determining the reactivity of metal surfaces. *Surf. Sci.* **1995**, *343*, 211–220. [[CrossRef](#)]
29. Kang, Y.; Snyder, J.; Chi, M.; Li, D.; More, K.L.; Markovic, N.M.; Stamenkovic, V.R. Multimetallic Core/Interlayer/Shell Nanostructures as Advanced Electrocatalysts. *Nano Lett.* **2014**, *14*, 6361–6367. [[CrossRef](#)]
30. Shen, L.-L.; Zhang, G.-R.; Miao, S.; Liu, J.; Xu, B.-Q. Core-Shell Nanostructured Au@NiPt₂ Electrocatalysts with Enhanced Activity and Durability for Oxygen Reduction Reaction. *ACS Catal.* **2016**, *6*, 1680–1690. [[CrossRef](#)]
31. Chen, H.Y.T.; Chou, J.P.; Lin, C.Y.; Hu, C.W.; Yang, Y.T.; Chen, T.Y. Heterogeneous Cu-Pd Binary Interface Boosts Stability and Mass Activity of Atomic Pt Clusters in the Oxygen Reduction Reaction. *Nanoscale* **2017**, *9*, 7207–7216. [[CrossRef](#)]
32. Zhuang, Y.; Chou, J.-P.; Tiffany Chen, H.-Y.; Hsu, Y.-Y.; Hu, C.-W.; Hu, A.; Chen, T.-Y. Atomic scale Pt decoration promises oxygen reduction properties of Co@Pd nanocatalysts in alkaline electrolytes for 310k redox cycles. *Sustain. Energy Fuels* **2018**, *2*, 946–957. [[CrossRef](#)]
33. Bhalothia, D.; Chou, J.-P.; Yan, C.; Hu, A.; Yang, Y.T.; Chen, T.Y. Programming ORR Activity of Ni/NiO_x@Pd Electrocatalysts via Controlling Depth of Surface-Decorated Atomic Pt Clusters. *ACS Omega* **2018**, *3*, 8733–8744. [[CrossRef](#)]
34. Bhalothia, D.; Lin, C.-Y.; Yan, C.; Yang, Y.-T.; Chen, T.-Y. Effects of Pt metal loading on the atomic restructure and oxygen reduction reaction performance of Pt-cluster decorated Cu@Pd electrocatalysts. *Sustain. Energy Fuels* **2019**. [[CrossRef](#)]
35. Dai, S.; Chou, J.-P.; Wang, K.-W.; Hsu, Y.-Y.; Hu, A.; Pan, X.; Chen, T.-Y. Platinum-trimer decorated cobalt-palladium core-shell nanocatalyst with promising performance for oxygen reduction reaction. *Nat. Commun.* **2019**, *10*, 440. [[CrossRef](#)] [[PubMed](#)]



© 2019 by the authors. Licensee MDPI, Basel, Switzerland. This article is an open access article distributed under the terms and conditions of the Creative Commons Attribution (CC BY) license (<http://creativecommons.org/licenses/by/4.0/>).